ELSEVIER

Journal of Fluids and Structures 24 (2008) 167–182

JOURNAL OF
FLUIDS AND
STRUCTURES

www.elsevier.com/locate/jfs

A strongly coupled, embedded-boundary method for fluid–structure interactions of elastically mounted rigid bodies

J. Yang[1], S. Preidikman[2], E. Balaras*

Department of Mechanical Engineering, University of Maryland, College Park, MD 20816, USA

Received 9 March 2006; accepted 4 August 2007
Available online 7 November 2007

Abstract

In the present paper, an embedded-boundary formulation that is applicable to fluid–structure interaction problems is presented. The Navier–Stokes equations for incompressible flow are solved on a Cartesian grid which is not aligned with the boundaries of a body that undergoes large-angle/large-displacement rigid body motions through the fixed grid. A strong-coupling scheme is adopted, where the fluid and the structure are treated as elements of a single dynamical system, and all of the governing equations are integrated simultaneously and interactively in the time domain. A demonstration of the accuracy and efficiency of the method is given for a variety of fluid–structure interaction problems.

Keywords: Fluid–structure interactions; Strong coupling; Incompressible flows; Embedded boundary method; Sharp interface; Finite difference method

---

1. Introduction

Numerical simulations of fluid flows interacting with dynamically moving boundaries are amongst the most challenging problems in computational mechanics. The main difficulty arises from the fact that the spatial domain occupied by the fluid changes with time and the location of the boundary is usually an unknown that depends on the fluid flow and the motion/deformation of the body. There is only a limited number of special cases where established boundary-conforming formulations can be directly applied with a relatively small overhead. The use of moving reference frames (Li et al., 2002), or coordinate transformations (Newman and Karniadakis, 1997; Shen et al., 2003) are characteristic examples. In more complex configurations, formulations utilizing moving and/or deforming grids that continuously adapt to the changing location of the body have to be adopted [see, for example, Tezduyar (2001), Hu et al. (2001), Glück et al. (2001)]. For problems that involve multiple bodies undergoing large motions and/or deformations, these algorithms are fairly complicated and have an adverse impact on the accuracy and efficiency of the fluid solvers.

---

*Corresponding author.
E-mail address: balaras@umd.edu (E. Balaras).

[1] Current address: IIHR-Hydroscience and Engineering, The University of Iowa, Iowa City, IA 52242, USA.

[2] Current address: Departamento de Estructuras, Universidad Nacional de Córdoba, (5000) Córdoba, Argentina.

0889-9746/$ - see front matter © 2007 Elsevier Ltd. All rights reserved.
doi:10.1016/j.jfluidstructs.2007.08.002

Recently, non-boundary conforming formulations have been increasingly gaining attention as tools to study fluid–structure interaction problems. A common feature of these methods is the solution of the Eulerian form of the Navier–Stokes equations on a fixed grid, and tracking of the moving body in a Lagrangian fashion. Consequently, the grid lines and the boundary of the body are almost never aligned. Their advantage compared to boundary-conforming formulations is that the need for regeneration and/or deformation of the grid is eliminated and, in most cases, standard structured or unstructured grid solvers can be used. On the other hand, the imposition of boundary conditions on the moving body is not trivial, and a variety of strategies with different degrees of accuracy and complexity have been developed over the years. Immersed boundary methods [see for example Peskin (1972)] or the distributed Lagrange multiplier (DLM) formulation [see Glowinski et al. (2001) and Dong et al. (2004)] are a few characteristic examples.

A class of methods that is particularly attractive for simulating laminar and turbulent flows in complex configurations is the embedded-boundary formulation introduced by Fadlun et al. (2000). The approach that was developed for fixed body problems, utilizes a pseudo-forcing function that is evaluated in the discrete space and is directly applied to the right-hand side (rhs) of the discretized momentum equations to satisfy the boundary conditions at the location of the body. The term pseudo-forcing is used because, in most cases, its addition to the rhs of the momentum equations is equivalent to the direct imposition of velocity boundary conditions within the solver (i.e. direct modification of the coefficients of the linear system). Subsequent applications utilized the above strategy to develop multi-dimensional reconstruction procedures so as to impose boundary conditions on complex stationary immersed boundaries in a variety of laminar and turbulent flows (Kim et al., 2001; Tseng and Ferziger, 2003; Balaras, 2004).

On the other hand, applications of the embedded-boundary methods to two-way, fluid–structure interaction problems, have been very limited. This is due to the additional complexity of such cases and also due to problems that are specific to the method. Compared to a stationary interface, for example, a moving interface introduces complications to the spatial-temporal integration of the governing equations, and therefore the estimation of the pseudo-forcing function becomes fairly complex. Although in Fadlun et al. (2000) the moving boundary problem of the flow inside an IC piston was demonstrated using their immersed boundary approach, the complexities brought in by moving interfaces on a fixed grid in a context of a time-splitting method were not addressed. Recently, Yang and Balaras (2006) proposed an embedded-boundary formulation applicable to moving boundary problems that gave very good results in a variety of laminar and turbulent flows. Central to their approach is a ‘field-extension’ procedure that extrapolates the flow field into the solid, thus assigning physical values to all the variables that belong to grid cells that will be emerging into the fluid. In all their computations, however, the boundary motion was prescribed. Uhlmann (2005) also used an embedded-boundary formulation to compute two-way, fluid–particle interactions. In contrast to the sharp interface formulation in Yang and Balaras (2006), he computed the pseudo-forcing on the Lagrangian markers rather than on the Eulerian grid points, and the necessary information transfer from the former to the latter (and *vice versa*) was carried out through a regularized delta function. The resulting time traces of the hydrodynamic forces on the particles were very smooth, and all his computations with an explicit coupling scheme were stable for density ratios down to $\rho_p/\rho_f = 1.2$ (where ρ_p and ρ_f are the densities of the solid particle and the fluid, respectively). A disadvantage is that the use of the regularized delta function compromises the sharpness of the interface, which substantially increases the resolution requirements even at low Reynolds numbers. Kim and Choi (2006) developed a strongly coupled algorithm for fluid–structure interactions in the framework of a sharp interface embedded-boundary method. To eliminate problems originating from the boundary motion, they used a non-inertial reference frame. The overall formulation also allowed for the solution of the coupled problem without an iterative procedure. A drawback of the approach, however, is that it is limited to fluid–structure interactions involving a single rigid body.

In the present study, we shall discuss a strategy to extend embedded-boundary formulations to fluid–structure interaction problems involving multiple bodies. Emphasis will be given on the coupling scheme, which is critical for the accuracy and efficiency of the overall method. In general, two different strategies can be adopted for the solution of the coupled system of equations governing the fluid and structural dynamics: monolithic and partitioned methods. In the former, both sets of equations are discretized with the same numerical method and the coupling conditions at the interface between the fluid and the structure are enforced within a single system of equations; the solution of this system gives both the fluid and the structural responses [see for example Hubner et al. (2004)]. On the other hand, partitioned methods can utilize different numerical methods for the fluid and structure systems, respectively. This gives more freedom in selecting suitable methods for fluid and structural solvers than the monolithic approaches. The partitioned approach can be further divided into weak-coupling and strong-coupling algorithms. The weak-coupling schemes are also called staggered methods due to the fact that equations governing the dynamics of the fluid and the structure are solved in an alternating manner. In this paper, we propose a strong-coupling scheme, where the fluid and the structure are treated as elements of a single dynamical system, and all the governing equations are integrated simultaneously and interactively in the time domain. The details of the numerical method are given in the next section. In the results section, problems with single and multiple bodies will be presented. In the former case, the parametric space is selected to mimic the conditions in reference experiments and simulations in the literature for the purpose of evaluating the accuracy and stability of the proposed formulation. In the latter case, periodic arrays of cylinders involving up to 32 degrees-of-freedom are considered in order to demonstrate the robustness and efficiency of the approach. A summary and conclusions will be given in the final section.

2. Problem formulation and numerical methods

The governing equations for unsteady incompressible viscous flow are:

$$\frac{\partial \mathbf{u}}{\partial t}+\nabla\cdot(\mathbf{u}\mathbf{u})=-\nabla p+\frac{1}{\mathrm{Re}}\nabla^2\mathbf{u}+\mathbf{f}, \tag{1}$$

$$\nabla\cdot\mathbf{u}=0, \tag{2}$$

where $\mathbf{u}$ is the velocity vector, t is the time, and p is the pressure; $\mathbf{f}$ represents a normalized external body force that will be used to enforce the desired velocity distribution over a solid boundary. The above equations have been made dimensionless using a reference velocity scale, U, and a reference length scale, L. The Reynolds number is defined as $\mathrm{Re}=UL/v$, where v the kinematic viscosity of the fluid.

The equation of motion that is generally used to model the motion of a two-dimensional, elastically mounted body, oscillating in the (x–y) plane has the form:

$$\mathbf{M}\ddot{\mathbf{x}}(t)+\mathbf{C}\dot{\mathbf{x}}(t)+\mathbf{K}\mathbf{x}(t)=\mathbf{F}(t), \tag{3}$$

where $[\,\dot{}\,]$ and $[\,\ddot{}\,]$ denote the first and second derivative with respect to time t, respectively, $\mathbf{M}$ is the mass matrix, $\mathbf{C}$ is the damping matrix, $\mathbf{K}$ is the stiffness matrix and $\mathbf{F}$ is the vector of generalized hydrodynamic forces per unit span applied by the fluid on the structure, and $\mathbf{x}(t)=X_0(t)\mathbf{i}+Y_0(t)\mathbf{j}+\Theta(t)\mathbf{k}$ is the vector of generalized structural displacements. Here, $X_0(t)$ and $Y_0(t)$ are the displacements of the center of mass of the body in the x and y directions, respectively, and $\Theta(t)$ is the rotation around z, an axis perpendicular to the (x,y) plane.

Eqs. (1) and (2), which govern the dynamics of the fluid, and Eq. (3), which governs the dynamics of the body, need to be solved in a coupled manner. A fundamental complication with two-way, fluid–structure interaction problems like the one described above, is that the prediction of the flow field and hydrodynamic loads requires knowledge of the motion of the structure and *vice versa*. In the present study, a strong-coupling scheme, based on Hamming's 4th-order, predictor–corrector method is used (Carnahan et al., 1969). Hamming's scheme was adapted to the present problem to avoid evaluating the hydrodynamic loads at fractional time-steps. In the following paragraphs, the fluid flow solver, the structural solver and the coupling scheme will be discussed in detail.

2.1. *Fluid flow solver*

Eqs. (1) and (2) are solved using a highly efficient fractional step method on a staggered Cartesian grid. All spatial derivatives are approximated using second-order central differences. The time stepping scheme is a second-order Adams–Bashforth scheme, where all terms in the rhs of momentum equations are advanced explicitly. The overall splitting scheme can be summarized as follows:

$$\frac{\hat{\mathbf{u}}^k-\mathbf{u}^{k-1}}{\Delta t}=(\mathrm{rhs})^k+\mathbf{f}^k=-\frac{3}{2}H(\mathbf{u}^{k-1})+\frac{1}{2}H(\mathbf{u}^{k-2})-\nabla p^{k-1}+\mathbf{f}^k, \tag{4}$$

$$\nabla^2\phi^k=\frac{1}{\Delta t}\nabla\cdot\hat{\mathbf{u}}^k, \tag{5}$$

$$\mathbf{u}^k=\hat{\mathbf{u}}^k-\Delta t\nabla\phi^k,\quad p^k=p^{k-1}+\phi^k, \tag{6,7}$$

where k is the timestep index, $\hat{\mathbf{u}}^k$ is the intermediate velocity, ϕ is the pressure correction, H is a spatial operator containing the convective and viscous terms, $\mathbf{f}^k$ is the discrete forcing function used to impose boundary conditions on an arbitrary immersed boundary that does not coincide with the underlying grid, and Δt is the time-step.

An immersed body moving on the fixed Cartesian grid is tracked in a Lagrangian manner using a series of marker particles. After establishing the grid-interface relation, all Cartesian grid nodes are split into the three categories shown in Fig. 1(a): (i) *fluid points*, which are points in the fluid phase; (ii) *forcing points*, which are grid points in the fluid phase with one or more neighboring points in the solid phase; and (iii) *solid points*, which are points in the solid phase. The

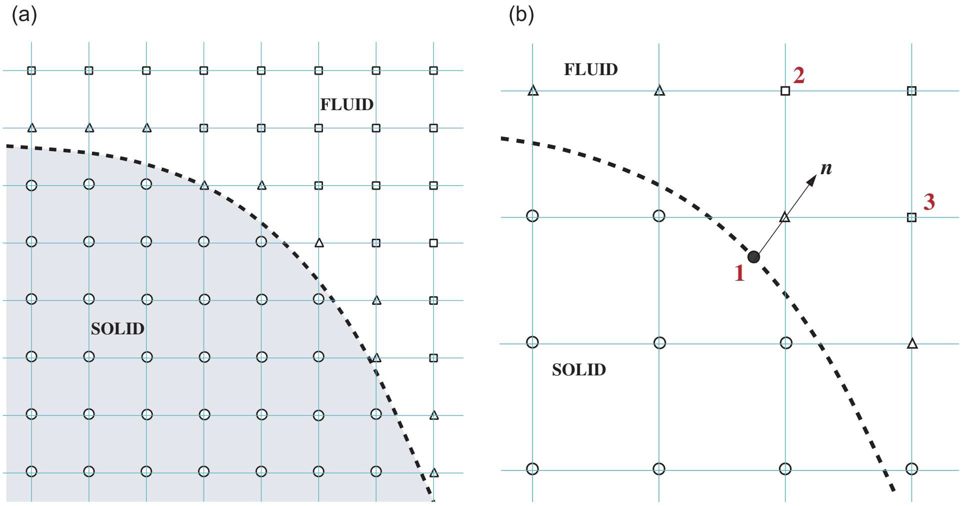

Fig. 1. (a) Tagging of grid nodes on the Eulerian grid according to their location relative to the fluid/solid interface indicated by the dashed line: ○, *solid points*; □, *fluid points*; △, *forcing points*. (b) Example of a linear local reconstruction stencil involving the projection of the forcing point to the interface (point 1) and two fluid points (points 2 and 3).

details of the tracking scheme and tagging procedure can be found in Balaras (2004). The Navier–Stokes solver described in the previous paragraph is applied on all points of the Eulerian grid as if the fluid/solid interface was not present. The effect of a moving solid body on the flow is introduced through the discrete forcing function, **f**. It is computed only at the forcing points by substituting $\hat{\mathbf{u}}^k$ with $\mathbf{u}_\Psi$ in Eq. (4) and solving for **f**:

$$\mathbf{f}^k = \frac{\mathbf{u}_\Psi - \mathbf{u}^{k-1}}{\Delta t} - (\mathrm{rhs})^k. \tag{8}$$

In the framework of the explicit fractional-step method discussed above, the use of **f**, given by Eq. (8), will enforce the proper boundary conditions on the predicted velocity, $\hat{\mathbf{u}}^k$. This choice does not compromise the overall temporal accuracy of the splitting scheme, and $\mathbf{u}^k$ will also satisfy the same boundary condition to the order of Δt^2. A more detailed discussion on this issue can be found in Kim et al. (2001) and Yang and Balaras (2006).

In the special case where the interface and the forcing point coincide, $\mathbf{u}_\Psi$ is simply the local velocity on the rigid body, and therefore the boundary condition one wishes to enforce. In the general case, however, the points on the Eulerian grid and the interface almost never coincide and $\mathbf{u}_\Psi$ has to be computed using some interpolation strategy. An example is shown in Fig. 1(b), where the velocity at the forcing point is computed by means of linear interpolation that involves the projection of the forcing point on the interface (point 1 in Fig. 1(b)) and two points in the fluid phase (points 2 and 3 in Fig. 1(b)). In the general case, the velocity or any variable, ψ, in the two-dimensional space can be approximated as follows:

$$\psi = b_1 + b_2 x + b_3 y. \tag{9}$$

The coefficients b_1, b_2, and b_3 in Eq. (9) can be found by solving the following system:

$$\begin{bmatrix} b_1 \\ b_2 \\ b_3 \end{bmatrix} = \mathbf{A}^{-1} \begin{vmatrix} \psi_1 \\ \psi_2 \\ \psi_3 \end{vmatrix} = \begin{bmatrix} 1 & x_1 & y_1 \\ 1 & x_2 & y_2 \\ 1 & x_3 & y_3 \end{bmatrix}^{-1} \begin{bmatrix} \psi_1 \\ \psi_2 \\ \psi_3 \end{bmatrix}, \tag{10}$$

where (x_1, y_1), (x_2, y_2), and (x_3, y_3) in the 3×3 matrix **A** are the coordinates of the three points in the interpolation stencil shown in Fig. 1(b). The inversion of matrix **A** at every forcing point is performed every time the location of the interface is updated. The above reconstruction strategy has been extensively tested for a variety of laminar and turbulent flow problems involving stationary and moving immersed boundaries with prescribed motion with results in excellent agreement with reference computations and experiments (Balaras, 2004; Yang and Balaras, 2006).

Both viscous and convective terms in the momentum equations are advanced in time using a second-order accurate, explicit Adams–Bashforth scheme. In our experience, except for very low Reynolds numbers, such a treatment does not require significantly smaller time-steps compared to semi-implicit approaches, and at the same time has two main advantages: it allows for a straightforward reconstruction of the velocity field around a moving immersed bodies while the parallelization of the overall solver is greatly simplified. A detailed discussion on this issue can be found in Yang and Balaras (2006). We should also mention that the overall coupling scheme proposed here can be used with fully implicit or semi-implicit formulations without any modification.

2.2. ODE Solver and strong-coupling scheme

Eq. (3) can be rewritten in nondimensional form, as a system of $2n$ first-order, nonlinear, ordinary differential equations (n is the number of degree-of-freedoms of the structure) as follows:

$$\dot{\mathbf{z}}(t) = \mathbf{q}(t), \tag{11}$$

where

$$\mathbf{z} = \begin{bmatrix} \tilde{\mathbf{x}} \\ \dot{\tilde{\mathbf{x}}} \end{bmatrix} \quad \text{and} \quad \mathbf{q} = \begin{bmatrix} \dot{\tilde{\mathbf{x}}} \\ \widetilde{\mathbf{F}} \end{bmatrix}, \tag{12}$$

with the first half of vector **z** and **q** representing the generalized displacements and the corresponding generalized velocities, while the other half of **z** and **q** for the generalized velocities and for the generalized forces divided by the corresponding inertias, respectively. In general, the loads depend explicitly on **z**, and implicitly on the history of the motion and the acceleration of the structure. Hamming's 4th-order, predictor–corrector method is used to integrate equation (11) in the time domain (Preidikman and Mook, 2000) . The details of the basic numerical procedure used to determine the current value of the vector **z** are given next:

(1) Let $t_j = j\Delta t$ denote the time at the jth time-step, where Δt is the time-step size used to obtain the numerical solution, and

$$\mathbf{z}^j = \mathbf{z}(t_j), \quad \dot{\mathbf{z}}^j = \dot{\mathbf{z}}(t_j), \quad \mathbf{q}^j = \mathbf{q}[\mathbf{z}(t_j)]. \tag{13}$$

(2) Compute the predicted solution, ${}^p\mathbf{z}^j$, and modify it, ${}^1\mathbf{z}^j$, using the local truncation error, $\mathbf{e}^{j-1}$, from the previous time-step:

$${}^p\mathbf{z}^j = \mathbf{z}^{j-4} + \tfrac{4}{3}\Delta t\ (2\mathbf{q}^{j-1} - \mathbf{q}^{j-2} + 2\ \mathbf{q}^{j-3}), \quad {}^1\mathbf{z}^j = {}^p\mathbf{z}^j + \tfrac{112}{9}\mathbf{e}^{j-1}. \tag{14}$$

(3) Correct the modified, predicted solution by

$${}^{k+1}\mathbf{z}^j = \tfrac{1}{8}[9\ \mathbf{z}^{j-1} - \mathbf{z}^{j-3} + 3\Delta t\ ({}^k\mathbf{q}^j + 2\ \mathbf{q}^{j-1} - \mathbf{q}^{j-2})], \tag{15}$$

where ${}^k\mathbf{q}^j = \mathbf{q}({}^k\mathbf{z}^j)$ and ${}^1\mathbf{z}^j = {}^p\mathbf{z}^j$. k is the iteration index. Convergence is achieved when the iteration error, $\Delta z^j = \|{}^{k+1}\mathbf{z}^j - {}^k\mathbf{z}^j\|_\infty$ is less than a prescribed tolerance ε.

(4) Compute the local truncation error, $\mathbf{e}^j$, and the final solution, $\mathbf{z}^j$, at step j and advance to the next time-step:

$$\mathbf{e}^j = \tfrac{9}{121}({}^{k+1}\mathbf{z}^j - {}^p\mathbf{z}^j), \quad \mathbf{z}^j = {}^{k+1}\mathbf{z}^j - \mathbf{e}^j. \tag{16}$$

The fluid solver described in Section 3.1 is coupled to the structural solver as follows:

(i) Find the predicted location and velocity of the body using Eq. (14).
(ii) Find the predicted fluid velocity and pressure fields using Eqs. (4)–(7) with the boundary conditions provided by step 1. Then, compute the resulting loads on the structure.
(iii) Compute the new location and velocity of the body using Eq. (15).
(iv) Check for convergence. If Δz^j is greater than the prescribed tolerance, ε, repeat steps 2–4. If convergence is achieved go to step 5.
(v) Find the final position and velocity of the body using Eq. (16), and the final fluid pressure and velocity fields from Eqs. (4)–(7).

In all computations reported in this study, a tolerance of $\varepsilon = 10^{-8}$ was used. The number of iterations required for convergence at each time-step varied from 2 to 6 depending on the problem.

To be able to compare the efficiency and robustness of the strong coupling scheme given above to weak coupling strategies, we also implemented an explicit coupling scheme, which utilizes an explicit, four-step, Adams–Bashforth method to predict the rigid body motion of the immersed bodies:

$$\mathbf{z}^j = \mathbf{z}^{j-1} + \frac{\Delta t}{24}(55\mathbf{q}^{j-1} - 59\mathbf{q}^{j-2} + 37\mathbf{q}^{j-3} - 9\mathbf{q}^{j-4}). \tag{17}$$

To start the calculation, an explicit Euler, two-step and three-step Adams–Bashforth methods are used for the first, second, and third time-step, respectively.

3. Results

To demonstrate the accuracy and efficiency of the proposed formulation, a series of test problems with increasing complexity is included. First, the problem of a circular cylinder undergoing free, transverse oscillations is considered. It is a problem that has been extensively studied both experimentally and numerically [see Williamson and Govardhan (2004) for a recent review], and therefore extensive data sets are available for comparison. The nondimensional form of Eq. (3) for the case of transverse oscillations, for example, can be written as follows:

$$\ddot{y} + 2\zeta\left(\frac{2\pi}{U^*}\right)\dot{y} + \left(\frac{2\pi}{U^*}\right)^2 y = \frac{2}{\pi m^*}C_L, \tag{18}$$

where the reduced velocity is defined as $U^* = U_\infty/f_N D$ with $f_N = (1/2\pi)\sqrt{k/m}$ the natural vibration frequency of the structure, and the mass ratio is defined as

$$m^* = \frac{m}{m_f} = \frac{m}{\rho_f \pi (D^2/4) L_c}, \tag{19}$$

with m_f the mass of the fluid replaced by the structure and ρ_f the fluid density, $y = Y_o/D$ is the nondimensionalized vertical displacement, $\zeta = c/2\sqrt{km}$ is the damping ratio, and $C_L = f_y/(\frac{1}{2}\rho D L_c U_\infty^2)$ is the lift force coefficient. In the above, m is system mass, c the damping coefficient, k the spring constant, Y_o the transverse displacement of the system centroid, L_c is the span of the cylinder, and f_y the instantaneous lift force on the cylinder. Note that the same reference scales as in the Navier–Stokes equations (the cylinder diameter, D, and the freestream velocity, U_∞) were used to obtain the dimensionless form of the equations of motion.

A high mass ratio, $m^* \sim 150$, is considered first in order to compare the simulation results to the low Reynolds number, two-dimensional, experiments by Anagnostopoulos and Bearman (1992). To investigate the robustness and accuracy of the method in cases where more complex modes of oscillation have been observed, low mass ratio cases ($1 < m^* < 10$), as well as oscillations in the (x, y) plane are considered. Highly accurate spectral simulation results are available in the literature for comparison [e.g. Blackburn and Karniadakis (1993), Leontini et al. (2006)]. Finally, to demonstrate the robustness of the method to multibody problems, vortex-induced vibrations of multiple cylinders (up to 16) are included.

3.1. Transverse oscillations of a circular cylinder: $m^* = 150$

The parametric space was selected to match the experiment by Anagnostopoulos and Bearman (1992), which has been used for validation in several other numerical simulations [see, for example, Nomura (1993), Wei et al. (1995), Schulz and Kallinderis (1998) and Li et al. (2002)]. The mass ratio was set to $m^* = 149.10$ and damping ratio to $\zeta = 0.0012$. The Reynolds number ranged from $\mathrm{Re} = 90$ to $\mathrm{Re} = 140$ and the corresponding reduced velocity from $U^* = 5.02$ to $U^* = 7.81$. A sketch of the computational domain is given in Fig. 2(a). The inflow boundary is located $10D$ upstream of the cylinder where a uniform velocity is specified. At the outflow boundary, located $30D$ downstream of the cylinder, a convective boundary condition is used (Orlanski, 1976). Radiative boundary conditions are used at both top and bottom boundaries (Gresho and Sani, 1987). The number of grid points in all computations was 320×240 in streamwise and transverse directions, respectively. The grid was stretched in both directions and the resulting resolution near the cylinder was approximately $0.02D \times 0.02D$. A detail of the grid is shown in Fig. 2(b). A constant time-step of $0.005D/U_\infty$ was used for all cases.

For all cases, the flow over a stationary cylinder for the same Reynolds number was initially computed. Then, the cylinder was allowed to move freely in the cross-stream direction. Integration in time was performed until a periodic state of constant maximum amplitude was reached. A major feature of vortex-induced vibrations is the so-called lock-in or synchronization phenomenon, which according to Khalak and Williamson (1999) is ‘the matching of the frequency

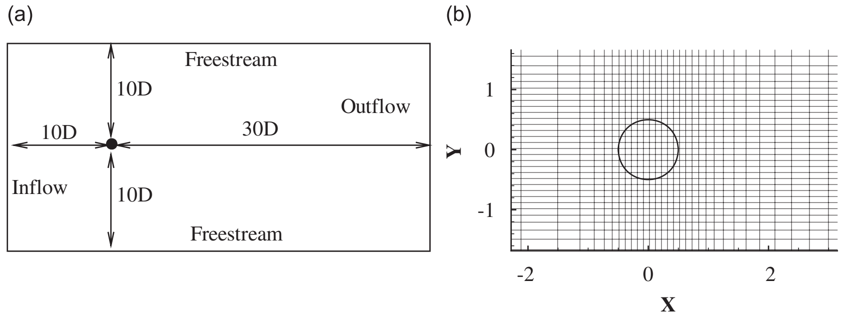

Fig. 2. Problem setup for the free vibrating cylinder in the cross-stream direction. (a) Sketch of the computational domain; (b) close-up of grid near the cylinder (every fifth point is shown).

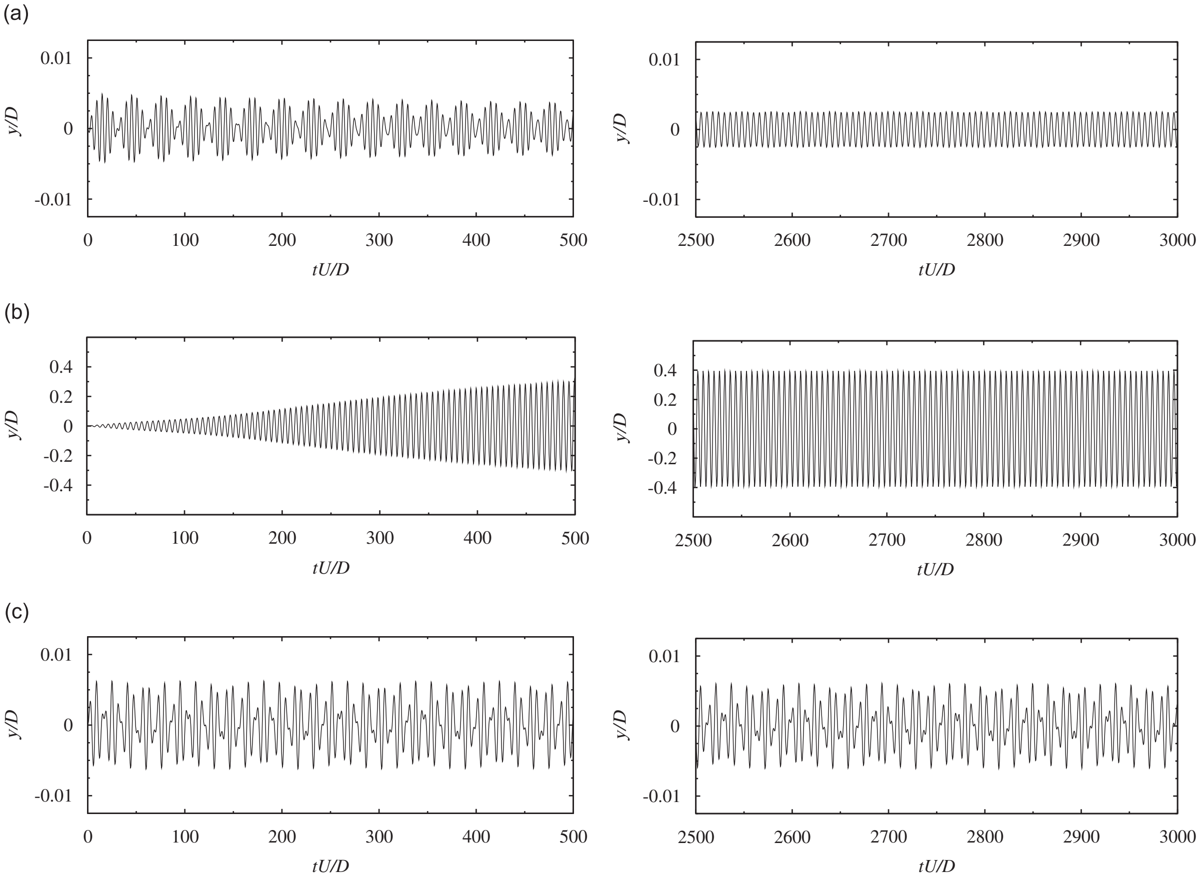

Fig. 3. Time history of the displacements for the freely vibrating cylinder in the cross-stream direction. Left column: start-up phase; right column: steady phase. (a) $\mathrm{Re} = 90$ ($U^* = 5.02$), (b) $\mathrm{Re} = 100$ ($U^* = 5.58$) and (c) $\mathrm{Re} = 140$ ($U^* = 7.81$).

of the periodic wake vortex mode with the body oscillation frequency'. For the large mass ratio cases considered here, in the lock-in regime the vortex shedding frequency also matches the natural vibration frequency of the cylinder. For all cases, approximately 2500 nondimensional time units were necessary for a periodic steady state to be reached. Based on the above definition, the lock-in regime ranges from $\mathrm{Re} = 95$ to 115 or $U^* = 5.30$ to 6.41 (see Fig. 4). It is interesting to note that the start-up phase is very different from case to case. At the lower end of the lock-in regime (i.e. $\mathrm{Re} = 100$, $U^* = 5.58$ shown in Fig. 3(b)), for example, oscillations of a monotonically growing amplitude can be observed. Outside the lock-in regime there is a drastic change in the vibration amplitude. At $\mathrm{Re} = 90$ ($U^* = 5.02$), modulated amplitude can be seen at start-up which reaches, however, a periodic steady state with a very small magnitude (see Fig. 3(a)). The cylinder oscillation frequency is $f_c = 0.165$, which is very close to vortex shedding frequency of the fixed cylinder at this Reynolds number. At higher reduced velocities also outside the lock-in regime (i.e., case $\mathrm{Re} = 140$, $U^* = 7.81$ shown in Fig. 3(c)), the displacement is still very low but its time history appears much more irregular than for the case with $U^* = 5.02$. Similar trends have been observed in the computations by Li et al. (2002).

The maximum oscillation amplitude and the corresponding frequency ratio between the vortex shedding and natural vibration frequencies are shown in Fig. 4 as functions of the Reynolds number and the reduced velocity. The experimental results in Anagnostopoulos and Bearman (1992) and previous computations (Nomura, 1993; Wei et al., 1995; Schulz and Kallinderis, 1998; Li et al., 2002) have been added for comparison. All reference computations have been conducted using boundary conforming formulations. In particular, Nomura (1993) and Wei et al. (1995) used an arbitrary Lagrangian–Eulerian (ALE) finite element formulation. The computational grid was deformed/regenerated to conform to the body at all times as the location of the cylinder changes. A similar strategy was used by Schulz and Kallinderis (1998) in the framework of a finite-volume formulation. There is some scatter in the results due to the complexity of the problem, different numerical methods, and grid resolution used in each simulation. Nevertheless, our results agree well (approximately within 2–5%) with those from Li et al. (2002) that have been obtained with a highly accurate spectral element method with a translating frame of reference without the error-prone process of mesh regeneration. Also, almost all simulations agree on the critical Reynolds number for lock-in (see Fig. 4(a)), which is however, lower compared to the one reported in the experiment. The corresponding values are approximately Re~95 in the simulations and Re~103 in the experiment. Schulz and Kallinderis (1998) speculated that this difference could be due to three-dimensional effects induced by the absence of end-plates in the experimental apparatus.

The vorticity contours for the case of maximum amplitude in the lock-in regime ($\mathrm{Re} = 95$, $U^* = 5.30$) are shown in Fig. 5. The expected 2S mode pattern (two single vortices per cycle of motion) can be seen in the wake, which is in agreement with the observations in Williamson and Roshko (1988).

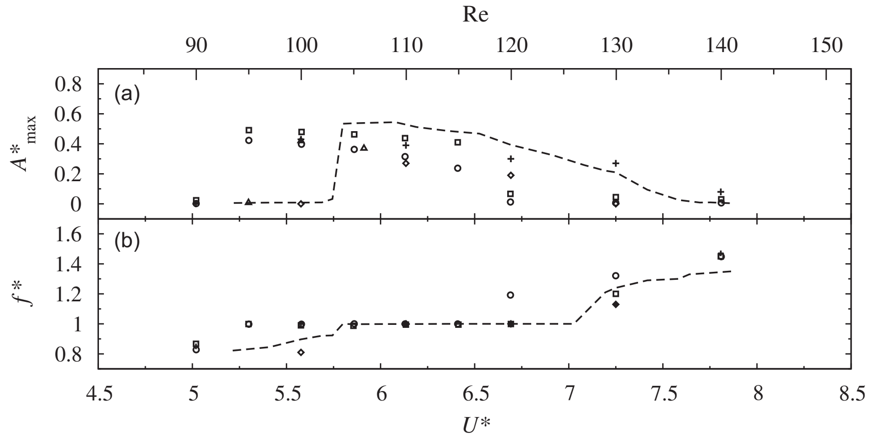

Fig. 4. Comparison of: (a) maximum oscillation amplitude $A^*_{\max}$; (b) frequency of the oscillation $f^* = f/f_N$, as a function of the reduced velocity. ○, Present computations; - - -, experiment in Anagnostopoulos and Bearman (1992); ◇, computation in Nomura (1993); +, computation in Wei et al. (1995); □, computation in Schulz and Kallinderis (1998); △, computation in Li et al. (2002).

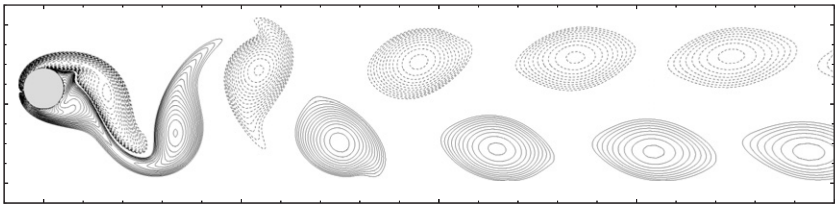

Fig. 5. Freely vibrating cylinder in the cross-stream direction: Spanwise vorticity isolines for case $\mathrm{Re} = 95$ ($U^* = 5.30$). Dashed lines indicate negative vosticity.

3.2. Transverse oscillations of a circular cylinder: $m^* = 10$

As the mass ratio, m^*, decreases, more complex oscillatory modes can appear. In a variety of experimental studies, two synchronous response branches have been found (Khalak and Williamson, 1999): (1) an upper branch which is characterized by a primary oscillation frequency close to that of the cylinder system, and a peak amplitude larger than one diameter. In addition, the phase angle between the lift force and the cylinder displacement is zero. (2) a lower branch which is characterized by an oscillation frequency which is higher than that of the cylinder system, and low peak amplitudes. The phase angle in this case is of the order of 180°. Such branching behavior has only been observed in high Reynolds number experiments and, therefore, has been closely associated to the three-dimensionality of the wake. In a recent study, however, Leontini et al. (2006) found evidence of such a branching behavior in lower Reynolds number, two-dimensional flow cases. In their two-dimensional spectral element computations, this was manifested by the sudden changes in the phase angle between the lift force and the cylinder displacement, although no differences were observed in the peak oscillation amplitude.

To demonstrate that the proposed formulation can capture this complex behavior, we conducted a series of simulations with parameters chosen from Leontini et al. (2006). The mass ratio was set to $m^* = 10$ and damping ratio to $\zeta = 0.01$. The Reynolds number is $\mathrm{Re} = 200$ and the reduced velocity ranges from $U^* = 4$ to $U^* = 7$. The boundary condition set-up and the size of the computational domain were kept the same as in the high mass ratio computations reported in the previous section. The number of grid points was set to 640×480 in streamwise and transverse directions, respectively. The grid was stretched in both directions and the resulting resolution near the cylinder was approximately $0.01D \times 0.01D$. A constant time-step of $0.004D/U_\infty$ was used for all cases.

In Fig. 6 the maximum oscillation amplitude, $A^*_{\max}$, the peak lift coefficient, $C_{L\max}$, the frequency of the oscillation, $f^* = f/f_N$, and the average phase angle between lift force and centerline displacement, ϕ, are shown as functions of the reduced velocity. The data from the spectral element computations of Leontini et al. (2006) are also included. The branching behavior manifested by the sudden jump of the phase angle and the sudden drop of maximum lift coefficient (see Fig. 6(d, c)) around $U^* = 4.7$ can also be seen in our computations. Also, the frequency ratio changes from below unity to unity and retains it until the system exits the lock-in regime at $U^* = 6.3$. Overall the agreement with the reference data is excellent (within 5%).

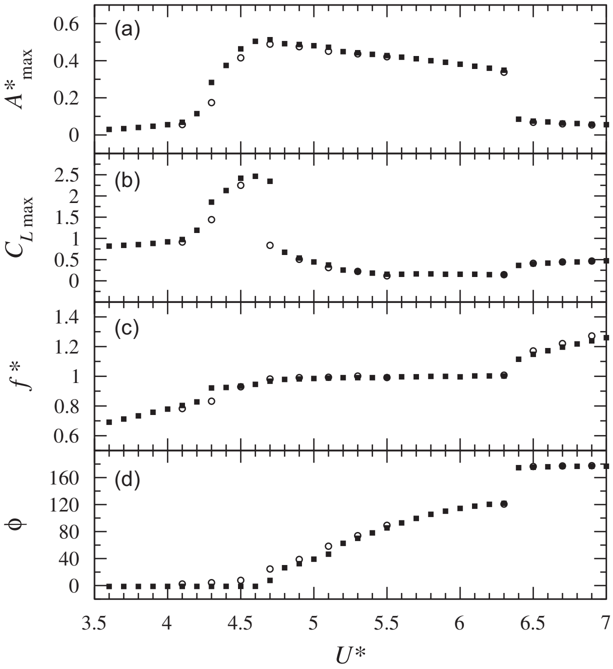

Fig. 6. Response of an elastically mounted circular cylinder as a function of the reduced velocity; $\mathrm{Re} = 200$, $m^* = 10$, $\zeta = 0.01$. (a) Maximum oscillation amplitude $A^*_{\max}$; (b) peak lift coefficient $C_{L\max}$; (c) frequency of the oscillation $f^* = f/f_N$; (d) average phase angle between lift force and centerline displacement. ○, Present computations; ■, computation in Leontini et al. (2006).

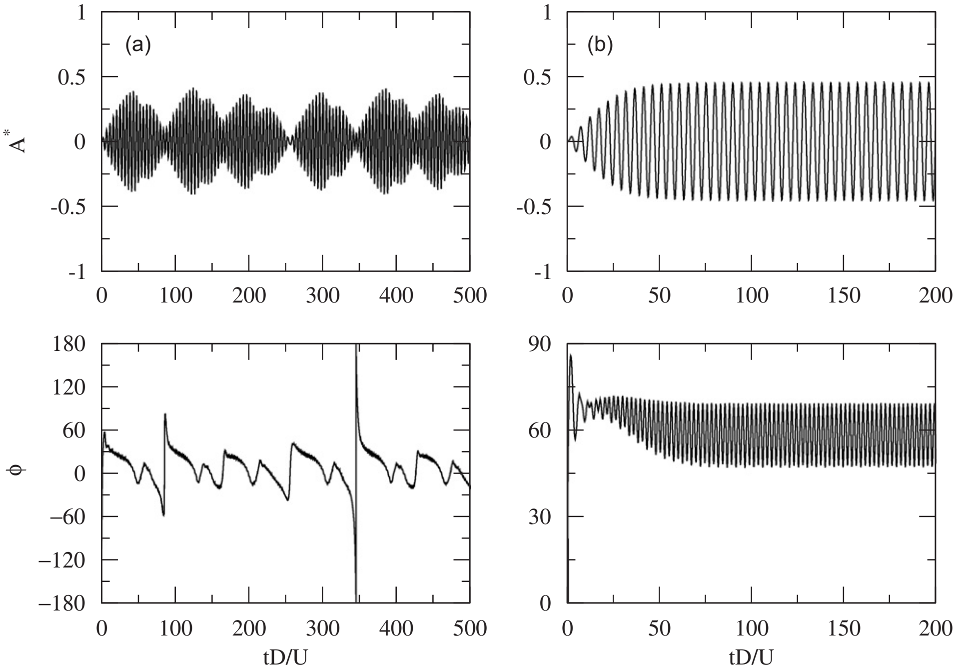

Fig. 7. Time series of cylinder displacement (top) and phase angle (bottom). Both variables computed as in Leontini et al. (2006). (a) Upper-type branch, $U^* = 4.5$; (b) lower-type branch, $U^* = 5.1$. For clarity different scales are used on both x and y axes.

The averaged quantities given in Fig. 6 that point to the presence of an upper-type and a lower-type branch are a direct manifestation of very different instantaneous dynamics. Leontini et al. (2006) reported that the behavior of the upper-type branch is not periodic and the amplitude of oscillation has a complex temporal variation. They also reported instantaneous phase angles, ϕ (Khalak and Williamson, 1999), which exhibit large fluctuations as they vary in line with the growth and decay of the displacement amplitude. As U^* increases and transition to the lower-type branch occurs, both A^* and ϕ become periodic. In our computations, this behavior has been accurately captured as it can be seen in Fig. 7 where the displacement and phase history for $U^* = 4.5$ (upper-type branch) $U^* = 5.1$ (lower-type branch) are shown. This further verifies that our approach can reproduce the complex dynamics with very good accuracy.

3.3. X–Y oscillations of a circular cylinder

All computations in Sections 3.1 and 3.2 were conducted with the strong-coupling scheme. We found that the explicit coupling scheme given by Eq. 17 is equally stable at least when similar timesteps are used. In many fluid–structure interaction problems, however, stability issues have been reported when the fluid equations are weakly coupled to the equations governing the motion for the structure. Hu et al. (2001), for example, demonstrated that for a weak coupling scheme, growing oscillations can arise when light spherical particles interact with the flow. Uhlmann (2005) found that the lower limit of the density ratio (density of particle versus the density of the fluid) or mass ratio as defined herein for stable computations of such flows is 1.05 for disks and 1.2 for spherical particles. Below these values, the weak-coupling scheme was found to be unstable. Glück et al. (2001) used a strong-coupling strategy to compute fluid–structure interactions of lightweight structures.

To compare the two coupling strategies, the case of a circular cylinder oscillating in the (x, y) plane was considered. The Reynolds number was set to Re $= 200$, the reduced velocity was $U^* = 5.0$, and the damping ratio was $\zeta = 0.01$. The mass ratio was varied between $0.5 \leqslant m^* \leqslant 4/\pi$. The computational domain and boundary condition set-up is similar to the one used for the vertically oscillating cylinder. The grid has been modified, however, to ensure appropriate resolution in the wider range of motion of the cylinder. The number of grid points in all computations was 400 × 360 in streamwise and transverse directions respectively, resulting in near cylinder resolution of approximately $0.02D \times 0.02D$. As for the previous case, in all computations the corresponding stationary cylinder problem was first solved and then free vibrations in both directions were allowed. Due to the low mass ratio in this case, a stable periodic state was achieved much faster compared to the previous problem.

We first considered the case of $m^* = 4/\pi$, which has also been computed by Blackburn and Karniadakis (1993) using a higher-order spectral element method with an accelerating reference frame. The predicted trajectory of the cylinder-center during the periodic steady state is shown in Fig. 8(a). Our results from both the strong- and weak-coupling schemes agree very well with the spectral simulation. In the latter, however, the center of the periodic, figure-eight-type oscillations is at $x = 0.62D$, referring to the coordinate system shown in Fig. 2(b). In our computations, the origin is slightly shifted downstream by $\delta x = 0.0185D$ due to a 3% difference in drag force. The overall temporal variation of the drag and lift coefficients (see Fig. 8(b,c)) is also in good agreement with the reference results.

Both the strong- and weak-coupling schemes were equally stable down to mass ratios of $m^* \sim 1.08$, and approached similar periodic steady-states. The differences in the trajectories of the center of the cylinder and the lift and drag coefficients were between 3% and 5%. For lower mass ratios, however, the weak-coupling scheme was found to be unstable. In Fig. 9(a), the x–y trajectories of the cylinder center are compared for $m^* = 1.07$. The strong-coupling scheme remains stable, and after the initial transient it reaches a periodic steady-state. In Fig. 10, the corresponding isolines of the vorticity and pressure are shown for an instant in time during the periodic steady state. The vortex pattern in the wake resembles the one that has been observed in a variety of experiments (Jauvtis and Williamson, 2004). The weak-coupling scheme, on the other hand, becomes unstable soon after the computation is initialized. Fig. 9(b) shows the large oscillations of the center of the cylinder that eventually lead to an exponential instability.

3.4. Free oscillations of multiple cylinders

In this section, we will present a series of fluid–structure interaction computations involving a periodic array of cylinders, where each cylinder is allowed to oscillate in the (x, y) plane. This is a challenging problem for any type of boundary conforming formulation, since the presence of multiple bodies undergoing large displacements makes the preservation of the grid quality a very complex task [see, for example, So et al. (2003)]. For the present methodology, grid generation is trivial since the requirement that the mesh conforms to the body is relaxed. As a coupled problem, however, the motion of each body depends on the flow and indirectly on the motion of all others, and this is a very stringent test for the robustness and efficiency of strongly coupled algorithms. To address this issue, we gradually increased the number of cylinders in the array from four to sixteen. In particular, three computations were conducted involving a 2×2, 3×3 and 4×4 array of cylinders as shown in Fig. 11(a). All cylinders have the same diameter, D,

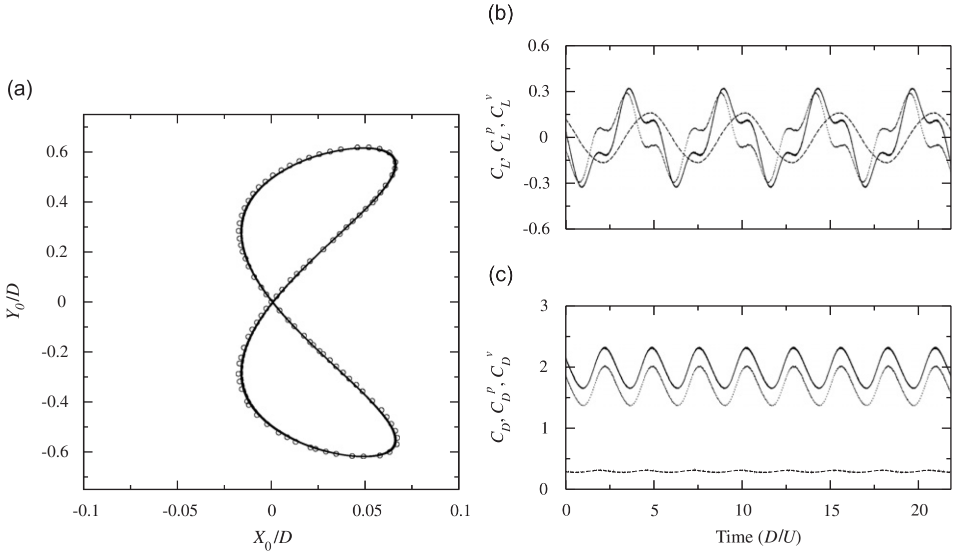

Fig. 8. Centerline displacement phase plot and time series of lift and drag coefficients for a circular cylinder freely vibrating in the (x, y) plane ($\mathrm{Re} = 200$, $U^* = 5.0$, $m^* = 4/\pi$). (a) Centerline displacement phase plot: ○, Blackburn and Karniadakis (1993); - - -, strong-coupling; ——, weak-coupling. (b) Lift coefficient and its pressure and shear stress components. (c) Drag coefficient and its pressure and shear stress components. In (b) and (c), only results from strong-coupling scheme are shown: ——, lift/Drag coefficients; · · · · · ·, pressure component; - - -, shear stress component.

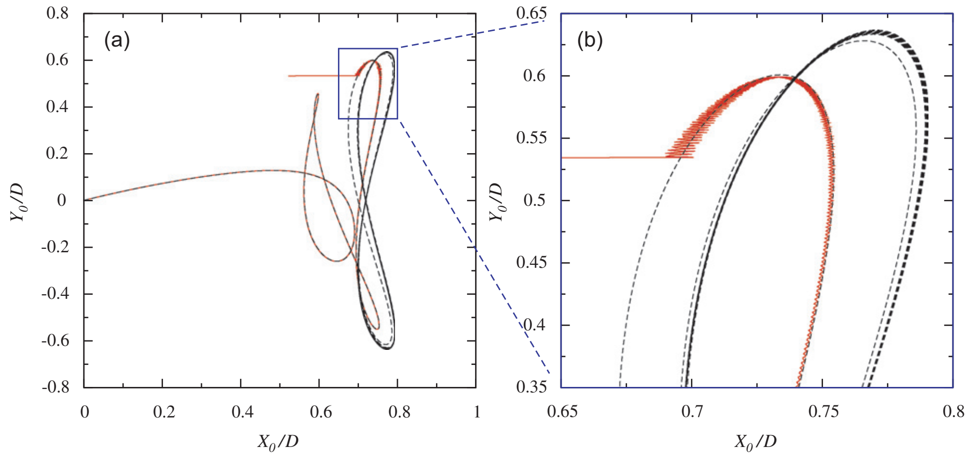

Fig. 9. Centerline displacement phase plot for a cylinder freely vibrating in the (x, y) plane (Re = 200, $U^* = 5.0$, $m^* = 1.07$): - - -, strong-coupling; ——, weak-coupling. (a) Complete trajectory; (b) zoom at the area where the weakly coupled scheme becomes unstable.

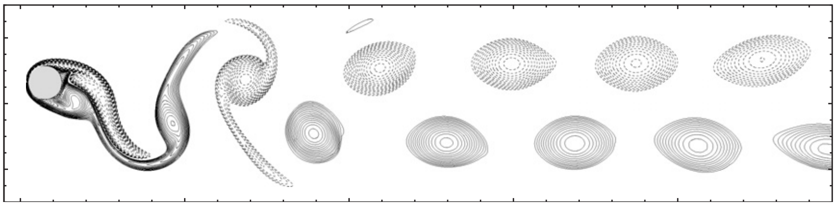

Fig. 10. Freely vibrating cylinder in the (x, y) plane: Spanwise vorticity isolines (dashed lines indicate negative vorticity) at Re = 200, $U^* = 5.0$, and $m^* = 1.07$. Strong-coupling scheme.

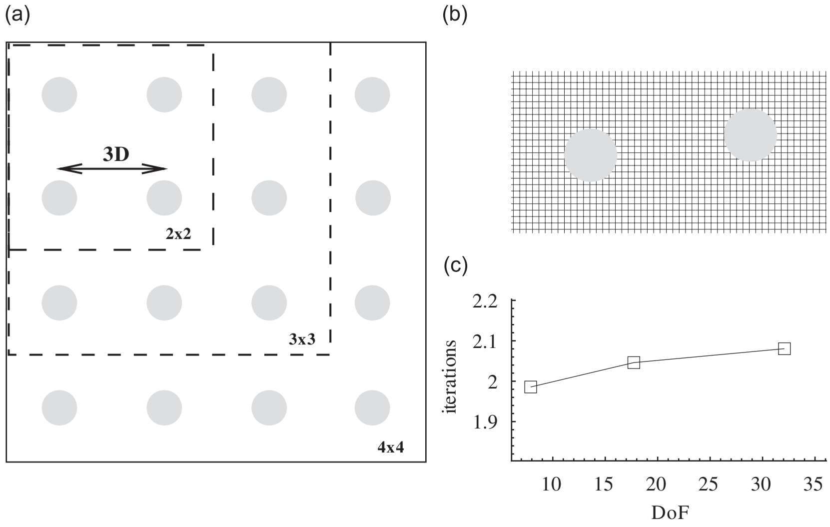

Fig. 11. Vortex-induced vibrations in a periodic array of cylinders. (a) Sketch of the computational domain for all cases. (b) Example: the underline Cartesian grid in the vicinity of the body (every fourth cell is shown). (c) Convergence of the predictor–corrector coupling scheme as a function of the number of degree-of-freedom.

and the distance between the centers of two consecutive cylinders is $3D$. For all cases, the Reynolds number was set to $\mathrm{Re} = U_b D/\nu = 200$ (U_b is the mean bulk velocity). The mass and damping ratio were set to $m^* = 12.73$ and $\zeta = 0.03$, respectively. The first (and unique) frequency of the system was selected such that $U^* = 5$. Periodic boundary conditions were used in both coordinate dimensions and a constant flowrate was imposed. All computations started with fixed cylinders. A uniform grid with $\Delta x = \Delta y = 0.02D$ was used in all cases (see Fig. 11(b)) and it was found to be sufficient to capture the dynamics of the flow.

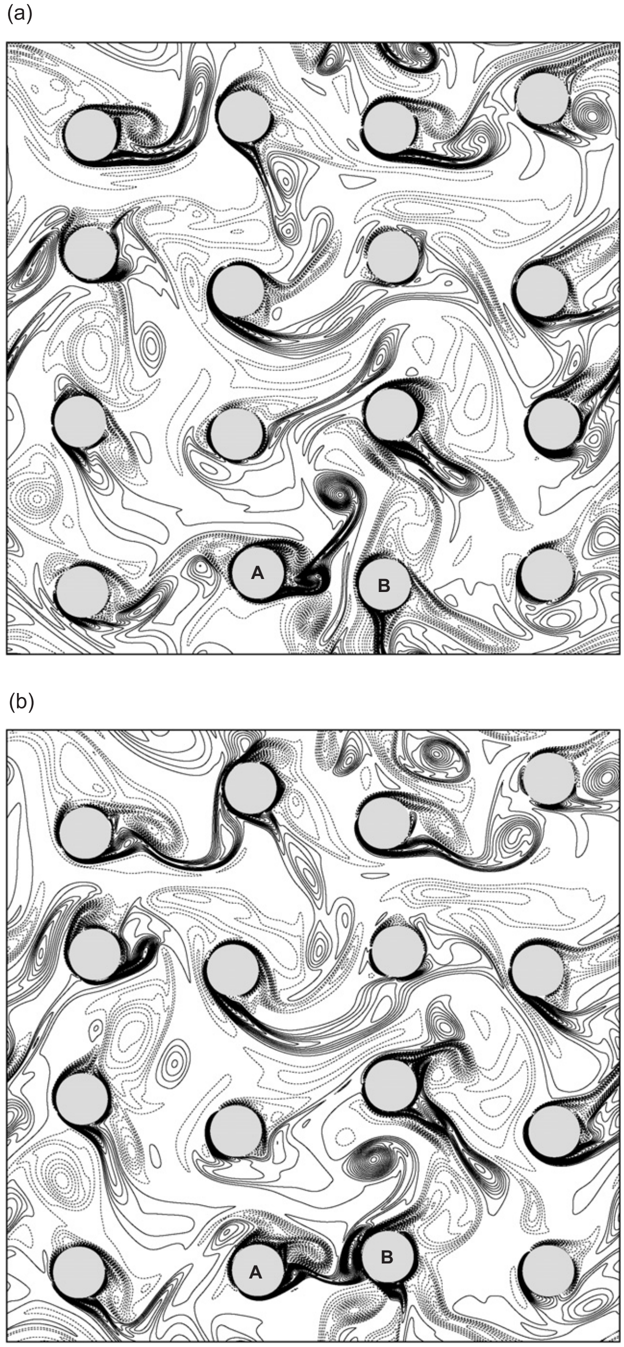

Fig. 12. Vortex induced vibrations in a periodic array of cylinders: Instantaneous vorticity isolines for the 4×4 array. (a) Time t_1; (b) time $t_2 > t_1$.

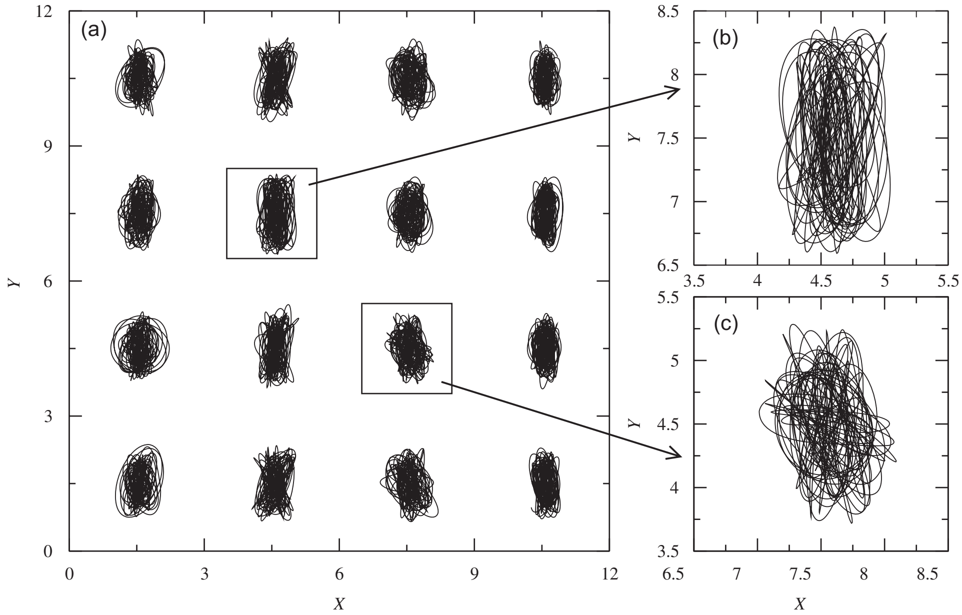

Fig. 13. (a) Trajectories of the center of each cylinder in the 4 array; (b) and (c) zoom in the region indicated in part (a).

Convergence of the predictor–corrector algorithm was found to be a very weak function of the number of cylinders. As shown in Fig. 11(c), the average numbers of iterations to achieve convergence ($\varepsilon < 10^{-8}$) in each time-step is approximately two and it is almost independent of the numbers of degrees of freedom, demonstrating the efficiency of our fluid–structure coupling scheme. The overall computational cost on the other hand depends on the number of bodies since the cost of interface tracking/reconstruction increases as the number of bodies increases. However, the cost is such that all the computations reported in this study can be performed on desktop workstations. The case with the 4 × 4 cylinder array for example, takes 3.4 s/iteration on an Intel Pentium D 3.00 GHz linux workstation. Given that the time-step is of the order of $\Delta t = 0.005D/U_b$, it takes a total of 1.8 CPU hours for a particle moving with the mean velocity to pass the computational domain.

The resulting flow fields for all cases were also very complex compared to vortex-induced vibrations of a single cylinder. In Fig. 12, isolines of vorticity for the 4 × 4 array are shown at one instant in time. In general, vortex shedding from the individual cylinders is not suppressed but is not as regular as in the case of isolated bodies. Vortices originating from a cylinder upstream interact with the neighboring cylinders and other vortices, generating a complex flow pattern. In Fig. 12(a) and (b), for example, where two consecutive instances are shown, a vortex pair originating from cylinder A interacts with cylinder B transferring some of its momentum to this cylinder but also altering the characteristics of the thin boundary layers on its surface. These complex patterns are also reflected in the trajectories of the centers of the cylinders, which were fairly chaotic and never reached a periodic steady state or some synchronized motion. In Fig. 13, these trajectories are shown for the 4 × 4 array for an arbitrary period of time. It is also worthwhile to note that the oscillation amplitude is much larger compared to the one in isolated oscillating cylinders; especially in the transversal direction, in some cases it approached $1D$.

4. Summary

In the present paper, an embedded-boundary formulation that is applicable to fluid–structure interaction problems is presented. The Navier–Stokes equations for incompressible flow are solved on a fixed grid and the body is tracked in a Lagrangian reference frame. A strong-coupling scheme is presented, where the fluid and the structure are treated as elements of a single dynamical system, and all of the governing equations are integrated simultaneously and interactively in the time domain. Results presented for cases of vortex-induced vibrations in a circular cylinder were in good agreement with reference data in the literature. Computations involving multiple bodies demonstrate the efficiency and robustness of the approach. We also demonstrate that a strong-coupling scheme is essential to the simulations of low mass ratio fluid–structure interaction problems, in which the weak coupling schemes usually fail.

Acknowledgments

EB and JY are supported by NIH Grant R01-HL-07262 and NSF Grant CTS-0347011.

References

Anagnostopoulos, P., Bearman, P.W., 1992. Response characteristics of a vortex-excited cylinder at low Reynolds numbers. Journal of Fluids and Structures 6, 39–50.

Balaras, E., 2004. Modeling complex boundaries using an external force field on fixed Cartesian grids in large-eddy simulations. Computers and Fluids 33, 375–404.

Blackburn, H.M., Karniadakis, G.E., 1993. Two- and three-dimensional simulations of vortex-induced vibration of a circular cylinder. In: Proceedings of the Third International Offshore and Polar Engineering Conference, Singapore, 6–11 June, 1993, pp. 715–720.

Carnahan, B., Luther, H.A., Wilkes, J.O., 1969. Applied Numerical Methods. Wiley, New York.

Dong, S., Liu, D., Maxey, M.R., Karniadakis, G.E., 2004. Spectral distributed Lagrange multiplier method: algorithm and benchmark tests. Journal of Computational Physics 195, 695–717.

Fadlun, E.A., Verzicco, R., Orlandi, P., Mohd-Yusof, J., 2000. Combined immersed-boundary finite-difference methods for three-dimensional complex flow simulations. Journal of Computational Physics 161, 35–60.

Glowinski, R., Pan, T.W., Hesla, T.I., Joseph, D.D., Périaux, J., 2001. A fictitious domain approach to the direct numerical simulation of incompressible viscous flow past moving migid modies: application to particulate flow. Journal of Computational Physics 169, 363–426.

Glück, M., Breuer, M., Durst, F., Halfmann, A., Rank, E., 2001. Computation of fluid–structure interaction on lightweight structures. Journal of Wind Engineering and Industrial Aerodynamics 89, 1351–1368.

Gresho, P.M., Sani, R.L., 1987. On pressure boundary conditions for the incompressible Navier–Stokes equations. International Journal for Numerical Methods in Fluids 7, 1111–1145.

Hubner, B., Walhorn, E., Dinkler, D., 2004. A monolithic approach to fluid–structure interaction using space–time finite elements. Computer Methods in Applied Mechanics and Engineering 193, 2087–2104.

Hu, H.H., Patankar, N.A., Zhu, M.Y., 2001. Direct numerical simulations of fluid–solid systems using the arbitrary Lagrangian–Eulerian technique. Journal of Computational Physics 169, 427–462.

Jauvtis, N., Williamson, C.H.K., 2004. The effect of two degrees of freedom on vortex-induced vibration at low mass and damping. Journal of Fluid Mechanics 509, 23–62.

Khalak, A., Williamson, C.H.K., 1999. Motions, forces and mode transitions in vortex-induced vibrations at low mass-damping. Journal of Fluids and Structures 13, 813–851.

Kim, J., Kim, D., Choi, H., 2001. An immersed-boundary finite-volume method for simulations of flow in complex geometries. Journal of Computational Physics 171, 132–150.

Kim, D., Choi, H., 2006. Immersed-boundary method for flow around an arbitrarily moving body. Journal of Computational Physics 212, 662–680.

Leontini, J.S., Thompson, M.C., Hourigan, K., 2006. The beginning of branching behavior of vortex-induced vibration during two-dimensional flow. Journal of Fluids and Structures 22, 857–864.

Li, L., Sherwin, S.J., Bearman, P.W., 2002. A moving frame of reference algorithm for fluid/structure interaction of rotating and translating bodies. International Journal for Numerical Methods in Fluids 38, 187–206.

Newman, D.J., Karniadakis, G.E., 1997. A direct numerical simulation study of flow past a freely vibrating cable. Journal of Fluid Mechanics 344, 95–136.

Nomura, T., 1993. Finite element analysis of vortex-induced vibrations of bluff cylinders. Journal of Wind Engineering and Industrial Aerodynamics 46–47, 595–604.

Orlanski, I., 1976. Simple boundary-condition for unbounded hyperbolic flows. Journal of Computational Physics 21, 251–269.

Peskin, C.S., 1972. Flow patterns around heart valves: a numerical method. Journal of Computational Physics 10, 252–271.

Preidikman, S., Mook, D.T., 2000. Time-domain simulations of linear and nonlinear aeroelastic behavior. Journal of Vibration and Control 6, 1135–1175.

Schulz, K.W., Kallinderis, Y., 1998. Unsteady flow structure interaction for incompressible flows using deformable hybrid grids. Journal of Computational Physics 143, 569–597.

Shen, L., Zhang, X., Yue, D.K.P., Triantafyllou, M.S., 2003. Turbulent flow over a flexible wall undergoing a streamwise traveling wave motion. Journal of Fluid Mechanics 484, 197–221.

So, R.M.C., Liu, Y., Lai, Y.G., 2003. Mesh shape preservation for flow-induced vibration problems. Journal of Fluids and Structures 18, 287–304.

Tezduyar, T.E., 2001. Finite element methods for flow problems with moving boundaries and interfaces. Archives of Computational Methods in Engineering 8, 83–130.

Tseng, Y.H., Ferziger, J.H., 2003. A ghost-cell immersed boundary method for flow in complex geometry. Journal of Computational Physics 192, 593–623.

Uhlmann, M., 2005. An immersed boundary method with direct forcing for the simulation of particulate flows. Journal of Computational Physics 209, 448–476.

Wei, R., Sekine, A., Shimura, M., 1995. Numerical analysis of 2D vortex-induced oscillations of a circular cylinder. International Journal for Numerical Methods in Fluids 21, 993–1005.

Williamson, C.H.K., Govardhan, R., 2004. Vortex-induced vibrations. Annual Review of Fluid Mechanics 36, 413–455.

Williamson, C.H.K., Roshko, A., 1988. Vortex formation in the wake of an oscillating cylinder. Journal of Fluids and Structures 2, 355–381.

Yang, J., Balaras, E., 2006. An embedded-boundary formulation for large-eddy simulation of turbulent flows interacting with moving boundaries. Journal of Computational Physics 215, 12–40.